An investigation of thermodynamics, microscopic structure, depolarized Rayleigh scattering, and collision dynamics in Xe-N_2 supercritical mixtures

D. Dellis[a], J. Samios[b], B. Collet[c], H. Versmold[c], J. Kłos[d], S. Marinakis[e,*]

[a]*Greek Research and Technology Network, Kifisias ave.7, 11523, Athens, Greece*
[b]*Laboratory of Physical Chemistry, Department of Chemistry, National and Kapodistrian University of Athens, Panepistimiopolis, Athens 15771, Greece*
[c]*Institute of Physical Chemistry, RWTH Aachen University, Landoltweg 2, 52056 Aachen, Germany*
[d]*Department of Chemistry and Biochemistry, University of Maryland, College Park, Maryland 20742-2021, USA*
[e]*Department of Chemistry and Biochemistry, School of Biological and Chemical Sciences, Queen Mary University of London, Joseph Priestley Building, Mile End Road, London E1 4NS, UK*

Abstract

Thermodynamics, microscopic structure and (single molecule and collective) dynamics in Xe-N_2 supercritical mixtures were studied using Molecular Dynamics simulations at a temperature of $T = 323\,\mathrm{K}$. The results agree well with previous experimental work on PVT-data and depolarized Rayleigh light scattering (DRLS). By using the corresponding DRLS time-correlation functions (TCFs), the contribution of orientational, interaction-induced and cross terms in the total DRLS TCF were evaluated. At all densities studied, the orientational part was found to be the most dominant. The Molecular Dynamics interaction potential model was compared with the most recent ab initio interaction potential energy surface (PES). Furthermore, quantum mechanical scattering calculations on the ab initio PES were used to provide integral and differential cross sections.

Keywords: Xenon, Nitrogen, Supercritical mixtures, Molecular dynamics, Depolarized Rayleigh scattering, Inelastic scattering

*Corresponding author
Email addresses: ntell@grnet.gr (D. Dellis), isamios@chem.uoa.gr (J. Samios), bernhard.collet@t-online.de (B. Collet), heinrich.versmold@gmx.de (H. Versmold), jklos@umd.edu (J. Kłos), s.marinakis@qmul.ac.uk (S. Marinakis)

1. Introduction

Supercritical fluids (SCF) have unique properties that have led to a rich variety of chemical applications including production of pharmaceutical products and essential oils, green chemistry, nuclear reactors and formation of nano- and micro-particles. Rare gases, nitrogen, carbon dioxide and water are among the most common supercritical (SC) systems. This work presents the first theoretical study that examines the density and concentration dependence of various properties in Xe-N_2 SC mixtures. The Xe-N_2 system has not been studied as extensively as the similar system Ar-N_2.

However, there is some previous work on this system. PVT data have been obtained by Brewer [1] and Collet [2]. Ewald [3] measured the solubility of solid Xe in compressed N_2 at 150 and 155 K, and Teller and Knapp [4] studied the solid-liquid equilibria for Xe-N_2 at temperatures between 91.0 and 160.4 K. Early work includes the measurements of thermal conductivity of Xe-N_2 at 30 and 45°C and pressure of 10 cm of Hg by Barua [5], and the theoretical estimations of thermal conductivities at 30°C based on diffusion coefficients [6]. Heymann and Kistemaker measured the thermal diffusion factors, α_T, at 300-700 K (20-40 cm Hg) using trace concentrations of radioactive ^{133}Xe [7]. Paul and Srivastava measured the mutual diffusion coefficient, D_{12}, between -30 and +60°C, and evaluated thermal conductivities between 242.2 and 334.2 K at pressures between 63.2 and 86.3 mm Hg [8]. Kistemaker and de Vries used acoustical absorption measurements to study the rotational relaxation in Xe + N_2 collisions [9]. The Xe-N_2 gas scintillators at high-pressures [10], and later [11] at low pressures have also been studied. Straub and Waibel used mixed Lennard-Jones (LJ) rules to describe the system [12], and Thomson [13, 14] used computer simulations to calculate diffusion coefficients, thermal diffusion coefficients, viscosity, and thermal conductivity at 303.16 K. His results were in good agreement with previous work on thermal conductivity [5, 6]. Trengove and Dunlop measured binary diffusion coefficient at 275-323 K, the concentration dependence of D_{12} at 300 K and 50 Torr, and thermal diffusion factors at 300 K and 30kPa [15]. A year later, they measured thermal diffusion factors at 253.29 and 274.24 K [16].

The first spectroscopic work was the measurement of the Far-infrared (FIR) absorption at room temperature and low densities by Guillot [17]. These measurements were later simulated by Roco et al. [18] who used quantum theory and a classical free linear rotor. Patrick et al. [19] measured electron drift velocities in Xe and Xe-N_2 mixtures. Although the Ar-N_2 van der Waals complex was observed by Herrebout et al. [20] using infrared spectroscopy, a similar attempt for the detection of Xe-N_2 at 80-123 K in the liquid phase was not successful. Aquilanti *et al.* [21] presented a theoretical study of the vibrationally selective electronic energy transfer in collisions of metastable Xe with N_2 molecules, and Cappelletti

et al. [22] measured absolute total cross sections for the ground (X $^1\Sigma_g^+$) and metastable state (A $^3\Sigma_u^+$) of N_2 in collisions with Xe. Aquilanti et al. [23] measured total (elastic+inelastic) cross sections for Xe-N_2 collisions for initial relative velocities up to 2300 m/s, i.e. at collision energies between 40 and 600 meV (323 - 4839 cm^{-1}). de Dios and Jameson [24] presented the first ab initio calculations of the ^{129}Xe nuclear shielding surfaces of Xe interacting with N_2, and the calculations from that work underestimated significantly the pressure virial coefficient.

Kooi et al. [25] measured a negative jump in the Raman shift in the nitrogen at the transition from the liquid to the solid phase in Xe; they explained that by analyzing the Xe-N_2 pair distribution functions for parallel and perpendicular geometries. Kooi and Schouten [26] used a high pressure (up to 13 GPa) Raman investigation of mutual solubility and van der Waals formation in Xe-N_2 at 408 K. Patton et al. [27] measured the chemical shift of hyperpolarized ^{129}Xe dissolved in liquid N_2.

Wen and Jäger [28] presented a microwave study of the Xe-N_2 accompanied by the most recent potential energy surfaces (PESs). The first PES, hereafter called PES-I, was constructed using coupled-cluster level of theory with single, double, and perturbatively included triple excitations [RCCSD(T)], and aug-cc-pVTZ basis sets with additional polarization functions for Xe. The second PES, hereafter called PES-II, employed the same level of theory but with a newly constructed aug-cc-pV5Z-PP basis set with small-core relativistic pseudopotentials for Xe. Both PES predicted a single minimum at a T-shaped geometry at an intermolecular separation R = 4.10 Å with well depths of 122.4 cm^{-1} (PES-I) and 119.3 cm^{-1} (PES-II). In order to achieve better agreement with the spectroscopic constants, Wen and Jäger scaled the PES. The best fit was achieved when they reduced the R by 0.058 Å and lowered the potential energy for the whole surface by $3.8\% \cdot (\cos\theta)$.

The present study aims to provide a joint computational and experimental investigation regarding thermodynamic, structural and dynamical properties of Xe-N_2. A particular reason for selecting this system was to investigate collision-induced phenomena in depolarized Rayleigh scattering of mixtures composed of a linear molecule, such as N_2, and a spherical molecule with high polarizability, such as Xe.

2. Computational Methods

2.1. Classical molecular dynamics (MD) simulations

The simulations were performed using an ensemble of 5324 molecules (N_2 and Xe) in a cubic box with the usual periodic conditions. The equations of motion were solved using the leapfrog algorithm. All MD calculations were performed with `DL_POLY` [29] package.

The simulations were carried out using LJ potential model for the Xe-Xe atoms and site-site LJ plus electrostatic terms using point charges for the N_2-N_2 interaction terms. The Xe potential parameters were adjusted to reproduce the experimental data of pure Xe at a wide range of densities and temperatures. The method described in [30] was used to optimize the Xe-Xe interactions. The quality of the derived Xe-Xe parameters in PVT data prediction is presented in Figure 1. The potential parameters for N_2 are those of ref. [31]. As mentioned by Mueller et al. [31], the electrostatic charges employed give a quadrupole moment which in absolute size is slightly lower than the experiment one in order to account for electrostatic induction. For the cross interactions the Lorentz-Berthelot combining rules were used. The runs were performed at mole fractions of N_2, $0.2 \leq x_{N_2} \leq 1$, at three densities (total concentrations) for each mole fraction where experimental data were available [2]. An initial run of 4×10^5 steps ($\sim$ 190 ps) was carried out followed by 10^6 steps ($\sim$ 472 ps) for the production run. The cut-off radius was 16 Å, and the standard Ewald summation technique has been used for the electrostatic interactions. The details of the simulations are summarized in Table 1.

Table 1: Interaction potential model, polarizabilities, and the simulated thermodynamic states of the mixtures.

Xe-Xe		
ϵ/k_B	[K]	222.11
σ	[Å]	3.9342
α [33]	[Å^3]	4.02
N-N		
Bond length	[Å]	1.098
ϵ/k_B	[K]	36.4
σ	[Å]	3.32
q_N	$\|e\|$	-0.408
q_{COM}	$\|e\|$	+0.816
α	[Å^3]	1.76
γ	[Å^3]	0.92
Time step	[fs]	0.4726
Thermodynamic states		
T	[K]	323
Total conc.	[mol/L]	6.5, 17.5, 22.5
x_{N_2}		0.2 - 1.0

Molecular Dynamics (MD) simulation together with experiment were used to study the depolarized Rayleigh light scattering (DRLS) of mixtures of Xe with N_2 at SC conditions. Results have been obtained for three different number densities

and six different mixture compositions at 323 K (see Table 2). It is well known that the depolarized Rayleigh light scattering in the conventional 90° scattering geometry (VH) [34] is given by the Fourier transform of the time-correlation function (TCF) of the second-rank part of the total polarizability **A** in the system [35–37]. The second-rank part of the polarizability tensor is given by

$$\mathbf{A}^{(2)} = \mathbf{A} - \mathrm{Tr}(\mathbf{A})\mathbf{1}/3 \tag{1}$$

The corresponding TCF can be written as:

$$C^{\mathrm{Ray}}(t) = \left\langle \mathbf{A}^{(2)}(0) : \mathbf{A}^{(2)}(t) \right\rangle \tag{2}$$

For a system composed of N molecules, the total polarizability can be written as a sum of the molecular polarizabilities $\boldsymbol{\alpha}$

$$\mathbf{A}^{(2)} = \sum_{i=1}^{N} \mathbf{A}_i^{(2)} = \sum_{i=1}^{N} (\boldsymbol{\alpha}_i^{(2)} + \Delta\boldsymbol{\alpha}_i^{(2)}) \tag{3}$$

where the molecular polarizability $\mathbf{A}_i^{(2)}$ is written as the sum of a permanent part and an induced part. The permanent part of the polarizability of a linear molecule can be written as [31]

$$\boldsymbol{\alpha} = \alpha\mathbf{1} + \boldsymbol{\alpha}_i^{(2)} = \alpha\mathbf{1} + \frac{2}{3}\gamma\boldsymbol{Q_i} \tag{4}$$

where α is the isotropic polarizability component, $\gamma = \alpha_{\parallel} - \alpha_{\perp}$ is the polarizability anisotropy, and if $\hat{u}$ is the unit vector parallel to the symmetry axis of the molecule, $Q_{\alpha\beta}$ is the $\alpha\beta$ element of **Q**

$$Q_{\alpha\beta} = \frac{1}{2}(3\hat{u}_{\alpha} \cdot \hat{u}_{\beta} - \delta_{\alpha\beta}). \tag{5}$$

For atoms like Xe, the molecular polarizability has only a scalar part. For a system containing N linear molecules the second-rank part of the collective polarizability can be written as:

$$\mathbf{A}^{(2)} = N\alpha\mathbf{1} + \frac{2}{3}\gamma \sum_{i=1}^{N} \mathbf{Q}_i \tag{6}$$

For simplicity we denote

$$\mathbf{Q} = \frac{2}{3}\gamma \sum_{i=1}^{N} Q_i \tag{7}$$

Thus, the second rank polarizability tensor of the system can be expressed as follows:

$$\mathbf{A}^{(2)} = \mathbf{Q} + \Delta\mathbf{A} \tag{8}$$

The depolarized Rayleigh correlation function will be written as (where we now drop the superscript (2) for clarity reasons):

$$C^{\mathrm{Ray}}(t) = \langle (\mathbf{Q}(0) + \Delta\boldsymbol{A}(0)) : (\mathbf{Q}(t) + \Delta\boldsymbol{A}(t)) \rangle \tag{9}$$

which can be reduced in three terms

$$C^{\mathrm{Ray}}(t) = \langle \boldsymbol{Q}(0) : \boldsymbol{Q}(t) \rangle + \langle \Delta\boldsymbol{A}(0) : \Delta\boldsymbol{A}(t) \rangle + \langle \boldsymbol{Q}(0) : \Delta A(t) + \boldsymbol{Q}(t) : \Delta\boldsymbol{A}(0) \rangle \tag{10}$$

The first term in Equation 10 depends only on the reorientation (OR) of the linear molecules, the second term on the collision-induced (CI) polarizability and the third is the cross (CR) correlation between the reorientational and interaction-induced parts. It is convenient to write the total correlation function as the sum of these terms [36]

$$C^{\mathrm{Ray}}(t) = C^{\mathrm{OR}}(t) + C^{\mathrm{CI}}(t) + C^{\mathrm{CR}}(t) \tag{11}$$

In order to calculate the total correlation function as well as its parts, we need a model for the calculation of the induced polarizability. The applied electric field induces on each molecule a dipole moment [38]

$$\mu_i = \alpha_i \left(\mathbf{E} + \sum_{j \neq i} \mathbf{T}_{ij} \cdot \alpha_j \right) \tag{12}$$

where $\mathbf{T}_{ij}$ is the dipole-induced dipole (DID) tensor [37]

$$\mathbf{T}_{ij}(r) = \frac{3\mathbf{r}_{ij}\mathbf{r}_{ij} - \mathbf{1}r_{ij}^2}{r_{ij}^5} \tag{13}$$

where $\mathbf{r}_{ij} = \mathbf{r}_i - \mathbf{r}_j$ is the intermolecular separation vector between molecules i and j. The induced dipole moment is linear in the field $\mathbf{E}$. Thus, for each molecule the induced dipole moment is proportional to the applied field and its effective polarizability tensor. Equation 12 represents a linear system of $3N$ linear equations that can be written in terms of the inverse matrix of the molecular polarizability of a molecule [39]

$$\sum_{j=1}^{N} B_{ij} \cdot \mu_j = \mathbf{E} \tag{14}$$

where B_{ij} is a symmetric tensor [39]

$$B_{ij} = \boldsymbol{\alpha}_i^{-1} \delta_{ij} - \mathbf{T}_{ij} \left(1 - \delta_{ij} \right) \tag{15}$$

$\boldsymbol{\alpha}_i^{-1}$ is the inverse matrix of the molecular polarizability of molecule j and $\mathbf{E}$ is the electric field in three dimensions. The system composed by equation 12 can

be solved accurately or using the first-order DID approximation [35, 36, 40–42] where the total induced polarizability in the system is given by equation

$$\Delta\boldsymbol{\alpha}_i = \sum_{i=1}^{N} \sum_{j \neq i}^{N} \boldsymbol{\alpha}_i \cdot \boldsymbol{T}_{ij} \cdot \boldsymbol{\alpha}_j \tag{16}$$

The first-order approximation is adequate for systems where the molecular polarizabilities are small, while a full solution is required for systems with high polarizability. The method that was used in this study was to solve the system of equations 12.

In this work, where the sample is a mixture that contains both linear and spherical molecules, the equations were modified for the absence of the rotational terms for atoms. The total polarizability of the system is

$$\boldsymbol{A} = N \left[x_{N_2} \alpha_{N_2} + (1 - x_{N_2}) \, \alpha_{Xe} \right] \mathbf{1} + \frac{2}{3} \gamma \sum_{i \in N_2} \mathbf{Q}_i \tag{17}$$

Light scattering time correlation functions, line shapes and intensities were computed using the all order exact DID model for the interaction-induced polarizabilities. The MD time correlation functions and the corresponding line shapes are analyzed, discussed and compared with experimental results at the same thermodynamic conditions.

2.2. Quantum Scattering Calculations

The PES used in this work was the scaled PES-I by Wen and Jäger [28]. The discrete data points of the potential represented on Jacobi radial and angular grid (R,θ) were fit using the reproducing kernel Hilbert space (RKHS) method [43]. The θ grid spanned values from 0 to 90 degrees with a step or 15 degrees. The radial grid contained 42 values between 3.442 and 9.942 Å. The radial-like kernel was chosen with $n = 2$ and $m = 5$ parameters to describe correctly R^{-6} asymptotic dependence and the angular-like kernel was composed of seven even-valued Legendre polynomials ($l_{max} = 12$) in a similar approach to work of Dryza *et al.* [44]. The RKHS fits are then used in Hibridon scattering program [45] with the $V_l(R)$ radial coefficients up to $l_{max} = 12$.

Contour plot of the PES is shown in Fig. 2. The kinetic energy of the system is 241 cm^{-1} at the temperature of 323 K employed in the experimental and Molecular Dynamics simulations. As shown in Fig. 2, this energy is located in the repulsive part of the PES. A similar contour plot for the classical interaction potential is shown in Fig. 3. A comparison between the quantum mechanical and classical interaction potential (Fig. 4) shows that the differences are very small around the T-geometry ($\theta = 90°$) and become larger at $\theta = 0°, 45°$ (and by symmetry at $\theta =$

135°, θ = 180°). The similarity between the classical and the quantum mechanical PESs allows the use of classical calculations to provide the ensemble average values for PVT and Rayleigh data at 323 K, and the use of quantum calculations for the state-to-state cross sections at the collision energy of 241 cm^{-1}, which corresponds to the temperature of the Rayleigh experiments.

Because of the nuclear spin of ^{14}N (I = 1), $^{14}N_2$ exists in separate *ortho* levels (with total nuclear spin I = 0 or 2) and *para* levels (with I = 1). The *ortho* to *para* ratio is 2:1, with the former populating only even (J = 0, 2, ...) levels, and the latter only odd (J = 1, 3, ...) levels. Close-coupling scattering calculations have been performed separately of *ortho* and *para* species using the HIBRIDON program [45] to provide integral (ICS) and differential (DCS) cross sections. The wavefunction was propagated between 4.5 and 18.8 a_0 using the improved log-derivative propagator by Manolopoulos and co-workers [46, 47]. We followed closely the methodology presented by Alexander in his study of Ar + N_2 collisions [48]. The N_2 molecule was described as a rigid rotor with rotational constant B = 1.989574 cm^{-1}. Calculations were performed for total energies up to 1435 and 1534 cm^{-1} for systems containing *ortho* and *para* systems. The maximum value of the total angular momentum was 300 and the maximum value of the rotational quantum number of the N_2 molecule was 35.

3. Results and discussion

3.1. Thermodynamics

The MD calculations successfully reproduce the experimental PVT data [2] and provided the values for the self-diffusion coefficients of both components in the mixture using the Einstein equation. Results for all the mole fractions are shown in Table 2.

3.2. Microscopic structure

The intermolecular structure of the mixture at these conditions has been studied in terms of the calculated pair distribution functions (g(r) or PDF) between the centre-of-mass (COM) of the molecules, between the sites of interactions, and between the sites and the COM. A clear second peak (of a lower intensity compared with the first one) in the g(r) indicates the formation of a second shell around molecule, and it is a clear manifestation of a liquid-like microscopic structure of an SCF. For example, the structure of SC-Xe has been studied previously (see ref. [49] and references therein). The existence of a clear first minimum in g(r) is often a sufficient evidence for liquid microscopic structure.

The PDFs for the N_2 COM - N_2 COM, N - N_2 COM, and N - N separations in Xe-N_2 mixtures at various total concentrations and mole fractions are shown in

Table 2: Experimental [2] and MD results for thermodynamic properties and self-diffusion coefficients of Xe-N_2 at 323 K.

C(M)	U_P (kJ/mol)	P_{MD} (bar)	P_{EXP} (bar)	D_{N_2} (10^{-9} m^2/s)	D_{Xe} (10^{-9} m^2/s)
			$x(N_2) = 0.00$		
6.5	-3.1537	91.4	90.2	-	39.31
17.5	-7.8296	470.4	464.5	-	9.39
22.5	-9.7177	1863	1859.7	-	4.38
			$x(N_2) = 0.20$		
6.5	-2.6068	113.1	114.0	94.0	43.5
17.5	-6.5404	534.0	547.5	16.61	11.93
22.5	-8.1501	1679.8	1693.2	7.73	6.22
			$x(N_2) = 0.35$		
6.5	-2.2167	129.5	131.9	96.78	46.47
17.5	-5.6435	584.2	610.1	21.60	12.92
22.5	-7.0474	1589.8	1601	11.50	8.10
			$x(N_2) = 0.50$		
6.5	-1.8711	142.1	146.7	97.57	53.75
17.5	-4.7881	641.5	670.3	23.67	16.31
22.5	-5.9971	1536.2	1574	13.56	10.33
			$x(N_2) = 0.77$		
6.5	-1.3129	165.6	172.4	107.4	70.37
17.5	-3.4162	728.4	765	29.72	19.28
22.5	-4.2740	1501.5	1551	18.80	13.54
			$x(N_2) = 0.95$		
6.5	-0.9890	179.7	182.9	120.17	78.83
17.5	-2.6030	780.5	780.2	35.07	26.19
22.5	-3.2599	1479.9	1455	22.78	16.52
			$x(N_2) = 1.00$		
6.5	-0.9028	183.8	185	137.77	-
17.5	-2.3893	796.5	781.3	38.17	-
22.5	-2.9893	1495.5	1430	26.07	-

Fig. 5. These PDFs have, in general, very similar shapes. For the lowest concentration (6.5 M), we observe a strong first peak and a weak second peak. For higher concentrations, we observe two clear peaks and a third weak one. The effect of the mole fraction is not important on the PDFs derived from this work. Regarding the height of the first peak, the order is N_2 - N_2 > N - N_2 > N - N. Regarding the

position of the first peak, the order is N - N < N - N_2 < N_2 - N_2. We refer to the work by Ling and Rigby [50], for a discussion of all the possible relative N_2 - N_2 orientations, and the important role of the X and T configurations.

The PDFs for the Xe - N_2 COM, Xe - N, and Xe - Xe separations of Xe-N_2 mixture at various concentrations and mole fractions are shown in Fig. 6. These PDFs have in general very similar shapes. As in the previous Figure, we have a strong first peak and a weak second peak for the lowest concentration. For higher concentrations, however, we have two clear peaks and a third weak one. The effect of the mole fraction is not important on the shape of these PDFs. Regarding the height of the first peak, the order is Xe-Xe > Xe - N_2 > Xe - N. Regarding the position of the first peak, the order is as follows: Xe - N < Xe - N_2 < Xe-Xe. This order is consistent with the corresponding order in the van der Waals radius, σ, between the interaction centers.

3.3. Depolarized Rayleigh scattering

Example of Rayleigh spectra for various total densities of a Xe-N_2 mixture for x_{N_2} = 0.2 are shown in Fig. 7 [2]. An increasing broadening effect is observed for increasing densities in the region of the Lorentz-like curve between 40 and 200 cm^{-1}. Note that at the lowest densities, the rotational resolution in the spectra is not lost and the relative intensity ratio between even and odd number is 2:1 because of the nuclear spin statistics of $^{14}N_2$ (see section 2.2).

In contrast to the behavior of the local microscopic structure, the DRLS is very sensitive to changes in concentration and mole fractions. The intensity of Rayleigh scattering versus wavelength for x_{N_2} = 0.2 is shown in Fig. 7 for concentrations between 0.275 and 22.5M [2]. A comparison between the fast Fourier transformed (FFT) experimental data and the MD time-correlation functions (TCFs) at T = 323 K is shown in Fig. 8 for the concentration of 6.5M. In general, the agreement between theory and experiment is better for lower mole fractions of nitrogen. The relatively good agreement between experimental and (total) theoretical TCFs gives support to the computational approach.

The MD calculations can separate the TCFs into re-orientational (OR), collision-induced (CI) and cross (CR) components as described in section 2.1. These components are shown in Fig. 9. The relative contribution from OR becomes more important for higher total concentrations and for higher N_2 mole fractions. In general, there are not many joint experimental and theoretical studies of the concentration dependence of DRLS (see ref. [51] for a study on CS_2/CCl_4 mixtures). Regarding pure N_2, our calculations are in agreement with the study by Mueller et al. [31], where they found that at low densities, the contributions are OR $\gg$ CI $\sim$ -CR, and at high densities OR $\gg$ -CR $\sim$ CI because in the latter case the sum of 2-body and 4-body terms is cancelled by the 3-body term. We also note that our results show that the OR term decays quicker than CI. This is similar to what is

observed in O_2, N_2 and Cl_2 [35, 36] but not in liquid CS_2 [52], possibly reflecting a much slower reorientation in the latter case.

3.4. Quantum integral and differential cross sections

A comparison between QM calculated ICS for Xe + *ortho*-N_2 (υ, $J = 0, 2$) and Xe + *para*-N_2 (υ, $J = 1, 3$) for various final N_2 rotational levels is shown in Fig. 10. The cross sections exhibit high values for the elastic collisions. Regarding the inelastic collision, they decrease with increasing energy gap between the initial and final levels. The behavior of ICSs is similar to those in Ar + N_2 collisions [48]. Future work will focus on obtaining the thermal rate coefficients from the cross sections.

The differential cross sections for Xe + *ortho*-N_2 (υ, $J = 0$) and Xe + *para*-N_2 (υ, $J = 1$) for various final N_2 rotational levels at a collision energy of 241 cm^{-1} are compared in Fig. 11. The DCSs exhibit a strong preference for forward scattering especially for low rotational excitations. They show oscillations due to interference like in the Ar + NO collisions [53]. In Xe + N_2, the oscillations are much more pronounced possibly because of the more homonuclear terms in the interaction potential compared with the Ar + NO, where heteronuclear terms also exist. Also, collisions with Xe will support more interferences with large angular momenta that pass through the long-range of the potential [54]. The amplitude of these oscillations generally decreases at higher scattering angles and for higher final N_2 rotational levels. Future work will provide information on the rotational alignment and on the kinetic energy dependence of the stereodynamics in the gas phase.

4. Conclusions

A new classical model for the interaction of Xe and N_2 was proposed and tested successfully in reproducing the thermodynamic data even at supercritical conditions. The MD calculations provided the microscopic structure of the mixture at various total concentrations (densities) and pressures at a temperature of 323 K. As it was expected, the microscopic structure was between gas-like and liquid-like. Also, the microscopic structure is more sensitive to the total concentrations than to the mole fractions of the mixture. The classical interaction potential from our new model was found very similar with the most recent ab initio PES [28].

The all order exact DID model was employed for the calculation of the interaction-induced polarizability. The Rayleigh spectra showed a very strong dependence on the N_2 mole fractions and the total concentration. The MD simulations were used to analyze the DRLS TCFs into re-orientational, collision-induced and cross components. For higher N_2 mole fractions, the collision-induced and cross components almost cancel each other. As the mole fraction of Xe increases, the contri-

bution of the interaction-induced term becomes greater and tends to be the main contribution in the total correlation function. For all densities studied, the long time ($t > 0.2$ ps) behaviour of the total correlation function is dominated by the interaction induced when $x_{N_2} \leqslant 0.5$. That means that the central part of the spectrum line shape is highly affected by the presence of Xe. We note that under similar experimental conditions, the Raman spectra of the mixture did not show any significant dependence on Xe [2]. An analysis of the TCFs in terms of compound-dependent contributions may be used for a comparison with a similar analysis for the CS_2/CCl_4 mixture [42].

Quantum mechanical scattering calculations were employed to provide state-to-state ICSs and DCSs for rotational excitation at a collision energy that corresponds to the temperature employed in the MD calculations and the experiments. We show that the ICSs decrease significantly when the energy gap between the initial and final rotational levels increases. Future work will provide the thermally averaged rate coefficients for these interactions. The DCSs show very pronounced oscillations, and we hope that this will prompt experimental measurements of the stereodynamics.

Acknowledgements

We would like to dedicate this work to the late Professor W. A. Steele (W.A.S.), Penn State University, USA. NATO Research-Project SA 5-2-05(CRG 950087) JARC (97) 288 is acknowledged for project funding to J.S., H.V. and W.A.S. The Greek State Scholarships Foundation (IKY) is acknowledged for an award based on performance to S. M. This work was supported by computational time granted from the Greek Research & Technology Network (GRNET) in the National HPC facility ARIS. The CPU time of the Computing Centre of the University of Athens (Greece) is gratefully acknowledged. This research utilized Queen Mary's Mid-Plus computational facilities, supported by QMUL Research-IT and funded by EPSRC grant EP/K000128/1. J.K. acknowledges financial support from the NSF Grant No. CHE-1565872 to Millard Alexander.

References

[1] J. Brewer, Determination of Mixed Virial Coefficients, Report No. MRL-2915-C; Air Force Office of Scientific Research, No. 67-2795, Report (1967).

[2] B. J. Collet, High-pressure Raman light scattering experiments on supercritical cyclopropane and nitrogen-xenon mixtures in a wide range of densities, PhD thesis, Institute of Physical Chemistry RWTH Aachen University

(2002).
URL http://publications.rwth-aachen.de/record/57135?ln=de

[3] A. H. Ewald, The solubility of solids in gases. Part 3.-The solubility of solid xenon and solid carbon dioxide, Trans. Faraday Soc. 51 (1955) 347–356. doi:10.1039/TF9555100347.

[4] M. Teller, H. Knapp, Measurements of solubilities of solid krypton and xenon in liquid nitrogen, Cryogenics 24 (1984) 471–476. doi:10.1016/0011-2275(84)90005-5.

[5] A. K. Barua, Thermal conductivity and Eucken type correction for binary mixtures of N_2 with some rare gases, Physica 25 (1959) 1275–1286. doi:10.1016/0031-8914(59)90049-7.

[6] S. Mathur, S. C. Saxena, Relations between thermal conductivity and diffusion coefficients of pure and mixed polyatomic gases, Proc. Phys. Soc. 89 (1966) 753. doi:10.1088/0370-1328/89/3/331.

[7] D. Heymann, J. Kistemaker, Thermal diffusion of xenon at tracer concentrations, Physica 25 (1959) 556–568. doi:10.1016/S0031-8914(59)95672-1.

[8] R. I. Paul, I. B. Srivastava, Studies on binary diffusion of the gas pairs N_2-Ar, N_2-Xe and N_2-He, Indian J. Phys. 35 (1961) 523–529.

[9] P. Kistemaker, A. E. de Vries, Rotational relaxation times in nitrogen-noble-gas mixtures, Chem. Phys. 7 (1975) 371–382. doi:10.1016/0301-0104(75)87020-0.

[10] W. Tornow, H. Huck, H.-J. Kber, G. Mertens, Properties of high pressure nitrogen-argon and nitrogen-xenon gas scintillators, Nucl. Instrum. Methods 133 (1976) 435. doi:10.1016/0029-554X(76)90427-4.

[11] T. Takahashi, S. Himi, M. Suzuki, J. Ruan, S. Kubota, Emission spectra from Ar-Xe, Ar-Kr, Ar-N_2, Ar-CH_4, Ar-CO_2 and Xe-N_2 gas scintillation proportional counters, Nucl. Instrum. Methods 205 (1983) 591–596. doi:10.1016/0167-5087(83)90028-5.

[12] D. Straub, R. Waibel, Zustandsgrößen und Transportkoeffizienten von binären Gasgemischen II Die Zweier-Wechselwirkung zwischen gleichen und ungleichen Molekülen, Chem. Eng. Sci. 28 (1973) 439. doi:10.1016/0009-2509(73)80042-9.

[13] R. M. Thomson, Calculations of the transport properties of dilute gas mixtures, Report, University of Leeds (1978).

[14] R. M. Thomson, Transport properties of dilute gas mixtures, Comput. Phys. Commun. 18 (1979) 123–132. doi:10.1016/0010-4655(79)90029-8.

[15] R. D. Trengove, P. J. Dunlop, Diffusion coefficients and thermal diffusion factors for five binary systems of nitrogen and a noble gas, Physica A 115 (1982) 339–352. doi:10.1016/0378-4371(82)90028-0.

[16] R. D. Trengove, P. J. Dunlop, The temperature dependence of the thermal diffusion factors of binary systems of nitrogen with the five noble gases and of helium with argon, Ber. Bunsenges. Phys. Chem. 87 (1983) 874–877. doi:10.1002/bbpc.19830871009.

[17] B. Guillot, P. Marteau, J. Obriot, Far-infrared absorption in nitrogen-rare gas compressed mixtures, Mol. Phys. 65 (1988) 765–784. doi:10.1080/00268978800101401.

[18] J. M. M. Roco, A. Calvo Hernández, S. Velasco, A. Medina, Many-body components in the integrated far-infrared absorption coefficient of diatomic molecules in spherical solvents, J. Chem. Phys. 107 (1997) 4844–4851. doi:10.1063/1.474847.

[19] E. L. Patrick, M. L. Andrews, A. Garscadden, Electron drift velocities in xenon and xenon-nitrogen gas mixtures, Appl. Phys. Lett. 59 (1991) 3239–3240. doi:10.1063/1.105744.

[20] W. A. Herrebout, A. A. Stolov, E. J. Sluyts, B. J. van der Veken, FTIR spectra of liquid argon/liquid nitrogen mixtures: evidence for the existence of a 1:1 bonded species $Ar{\cdot}N_2$, Chem. Phys. Lett. 295 (1998) 223–229. doi:10.1016/S0009-2614(98)00958-0.

[21] V. Aquilanti, R. Candori, F. Pirani, C. Ottinger, On the dynamics of the vibrationally selective electronic energy transfer from metastable xenon atoms to nitrogen molecules, Chem. Phys. 187 (1994) 171–183. doi:10.1016/0301-0104(94)00168-5.

[22] D. Cappelletti, G. Liuti, E. Luzzatti, F. Pirani, Characterization of a molecular beam containing metastable nitrogen and its use in scattering experiments with xenon, J. Chem. Phys. 101 (1994) 1225–1230. doi:10.1063/1.467815.

[23] V. Aquilanti, D. Ascenzi, D. Cappelletti, R. Fedeli, F. Pirani, Molecular beam scattering of nitrogen molecules in supersonic seeded beams: A probe of rotational alignment, J. Phys. Chem. A 101 (1997) 7648–7656. doi:10.1021/jp971237t.

[24] A. C. de Dios, C. J. Jameson, The ^{129}Xe nuclear shielding surfaces for Xe interacting with linear molecules CO_2, N_2, and CO, J. Chem. Phys. 107 (1997) 4253–4270. doi:10.1063/1.474800.

[25] M. E. Kooi, J. P. J. Michels, J. A. Schouten, Negative vibrational shift of nitrogen diluted in xenon at the fluid-solid transition, J. Chem. Phys. 110 (1999) 3023–3025. doi:10.1063/1.477896.

[26] M. E. Kooi, J. A. Schouten, High-pressure Raman investigation of mutual solubility and compound formation in Xe-N_2 and Ne-N_2, Phys. Rev. B 60 (1999) 12635–12643. doi:10.1103/PhysRevB.60.12635.

[27] B. Patton, N. N. Kuzma, W. Happer, Chemical shift of hyperpolarized ^{129}Xe dissolved in liquid nitrogen, Phys. Rev. B 65 (2001) 020404. doi:10.1103/PhysRevB.65.020404.

[28] Q. Wen, W. Jäger, Microwave spectra of the Xe-N_2 van der Waals complex: A comparison of experiment and theory, J. Chem. Phys. 122 (2005) 214310. doi:10.1063/1.1925274.

[29] DL_POLY is a molecular dynamics simulation package written by W. Smith, T.R. Forester and I.T. Todorov and has been obtained from STFC's Daresbury Laboratory via the website http://www.ccp5.ac.uk/DL_POLY.

[30] D. Dellis, J. Samios, Molecular force field investigation for sulfur hexafluoride: A computer simulation study, Fluid Phase Equilib. 291 (2010) 81–89. doi:10.1016/j.fluid.2009.12.018.

[31] A. Mueller, W. A. Steele, H. Versmold, Computer simulation study of the Rayleigh and Raman spectra of fluid N_2, J. Chem. Phys. 99 (1993) 4993–5001. doi:10.1063/1.466001.

[32] E. W. Lemmon, M. O. McLinden and D. G. Friend (2005), Thermophysical Properties of Fluid Systems, in NIST Chemistry WebBook, NIST Standard Reference Database Number 69, ed. P. J. Linstrom and W. G. Mallard, National Institute of Standards and Technology, Gaithersburg MD, 20899.http://webbook.nist.gov.

[33] C. G. Gray, K. Gubbins, Theory of molecular liquids, Clarendon Press, Oxford, 1984.

[34] B. J. Berne, R. Pecora, Dynamic Light Scattering, John Wiley, New York, 1976.

[35] D. Frenkel, J. P. McTague, Molecular dynamics studies of orientational and collision-induced light scattering in molecular fluids, J. Chem. Phys. 72 (1980) 2801–2818. doi:10.1063/1.439429.

[36] B. M. Ladanyi, Molecular dynamics study of Rayleigh light scattering from molecular fluids, J. Chem. Phys. 78 (1983) 2189–2203. doi:10.1063/1.445062.

[37] M. Keller, A. Mueller, W. A. Steele, Computer simulation study of Rayleigh and Raman spectra and spectral moments of fluid C_2H_6, J. Chem. Phys. 103 (1995) 8854–8863. doi:10.1063/1.470074.

[38] T. W. Zerda, X. Song, J. Jonas, B. M. Ladanyi, L. C. Geiger, Experimental and molecular dynamics study of depolarized Rayleigh scattering by O_2, J. Chem. Phys. 87 (1987) 840–851. doi:10.1063/1.453291.

[39] L. C. Geiger, B. M. Ladanyi, Higher order interaction-induced effects on Rayleigh light scattering by molecular liquids, J. Chem. Phys. 87 (1987) 191–202. doi:10.1063/1.453614.

[40] P. A. Madden, Interaction-induced phenomena in Proceedings of the NATO Advanced Study Institute on Molecular Liquids - Dynamics and Interactions, Florence, Italy, 1983, published in Molecular Liquids: Dynamics and Interactions, eds. A. J. Barnes, W. J. Orville-Thomas and J. Yarwood, NATO ASI Series C Vol. 135, 1984, pp. 431-474.

[41] G. Birnbaum, Phenomena Induced by Intermolecular Interactions, Plenum, New York, 1985.

[42] H. Stassen, U. Mittag and J. Samios, MD simulation of depolarized Rayleigh and FIR spectra in binary liquid mixtures in Proceedings of the NATO Advanced Study Institute on Molecular Liquids: New Perspectives in Physics and Chemistry, Luso, Portugal, 1991, published in Molecular Liquids: New Perspectives in Physics and Chemistry, ed. J. J. C. Teixeira-Dias, NATO ASI Series C Vol. 379, 1992, pp. 549-568.

[43] T. Ho, H. Rabitz, A general method for constructing multidimensional molecular potential energy surfaces from *ab initio* calculations, J. Chem. Phys. 104 (1996) 2584–2597. doi:10.1063/1.470984.

[44] V. Dryza, E. J. Bieske, A. A. Buchachenko, J. Kłos, Potential energy surface and rovibrational calculations for the Mg^+-H_2 and Mg^+-D_2 complexes, J. Chem. Phys. 134 (2011) 044310. doi:10.1063/1.3530800.

[45] The HIBRIDON package (version 4.4) was written by M. H. Alexander, D. E. Manolopoulos, H.-J. Werner, B. Follmeg, and P. Dagdigian with contributions by D. Lemoine, P. F. Vohralik, G. Corey, R. Gordon, B. Johnson, T. Orlikowski, A. Berning, A. Degli-Esposti, C. Rist, B. Pouilly, J. Kłos, Q. Ma, G. van der Sanden, M. Yang, F. de Weerd, S. Gregurick, and F. Lique, http://www2.chem.umd.edu/groups/alexander/.

[46] D. E. Manolopoulos, An improved log derivative method for inelastic scattering, J. Chem. Phys. 85 (1986) 6425–6429. doi:10.1063/1.451472.

[47] M. H. Alexander, D. E. Manolopoulos, A stable linear reference potential algorithm for solution of the quantum close-coupled equations in molecular scattering theory, J. Chem. Phys. 86 (1987) 20442050. doi:10.1063/1.452154.

[48] M. H. Alexander, Close-coupling studies of the orientation dependence of rotationally inelastic collisions, J. Chem. Phys. 67 (1977) 2703–2712. doi:10.1063/1.435184.

[49] S. Marinakis, J. Samios, The temperature and density dependence of fluid xenon self-diffusion coefficients: a comparison between experimental, theoretical and molecular dynamics results, J. Supercrit. Fluids 34 (2005) 81–89. doi:10.1016/j.supflu.2004.10.002.

[50] M. S. H. Ling, M. Rigby, Towards an intermolecular potential for nitrogen, Mol. Phys. 51 (1984) 855. doi:10.1080/00268978400100571.

[51] F. Strehle, T. Dorfmüller, J. Samios, Concentration effects on collision-induced depolarized Rayleigh lineshapes in CS_2/CCl_4 mixtures, Mol. Phys. 72 (1991) 993–997. doi:10.1080/00268979100100731.

[52] P. A. Madden, D. J. Tildesley, Interaction-induced contributions to Rayleigh and allowed Raman bands, Mol. Phys. 55 (1985) 969–998. doi:10.1080/00268978500101831.

[53] C. J. Eyles, M. Brouard, C.-H. Yang, J. Kłos, F. J. Aoiz, A. Gijsbertsen, A. E. Wiskerke, S. Stolte, Interference structures in the differential cross-sections for inelastic scattering of NO by Ar, Nat. Chem. 3 (2011) 597–602. doi:10.1038/nchem.1071.

[54] F. J. Aoiz, J. E. Verdasco, M. Brouard, J. Kłos, S. Marinakis, Inelastic scattering of He atoms and NO($X^2\Pi$) molecules: The role of parity on the differential cross section, J. Phys. Chem. A 113 (2009) 14636–14639. doi:10.1021/jp9043732.

Figure 1: Comparison between experimental data (lines) from ref. [32] for the pressure as a function of molar volume at various temperatures with simulation results (points) obtained using the optimized Xe-Xe LJ parameters from this work.

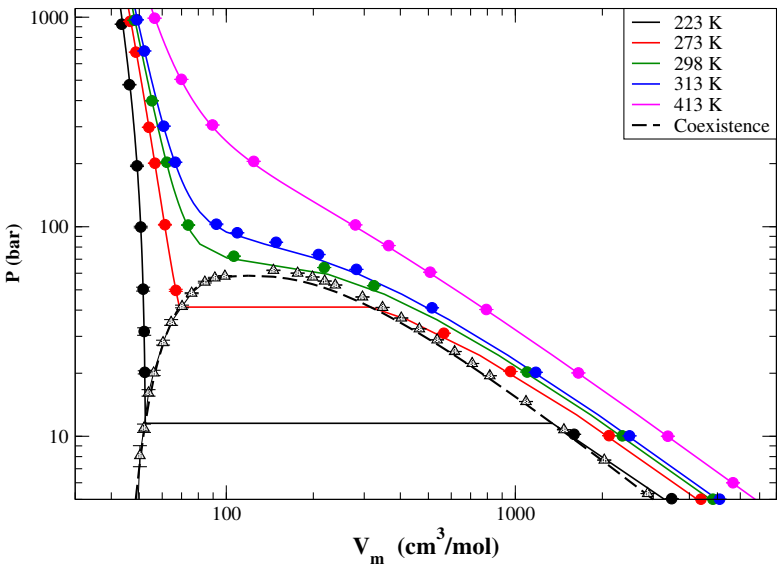

Figure 2: Contour diagram of the scaled PES-I ab initio Xe-N_2 potential energy surface [28] employed in the quantum scattering calculations. As indicated by the labeled contours, black lines represent positive values (repulsive part of the potential); blue lines are negative values. The contour line in red represent the collision energy of the present study.

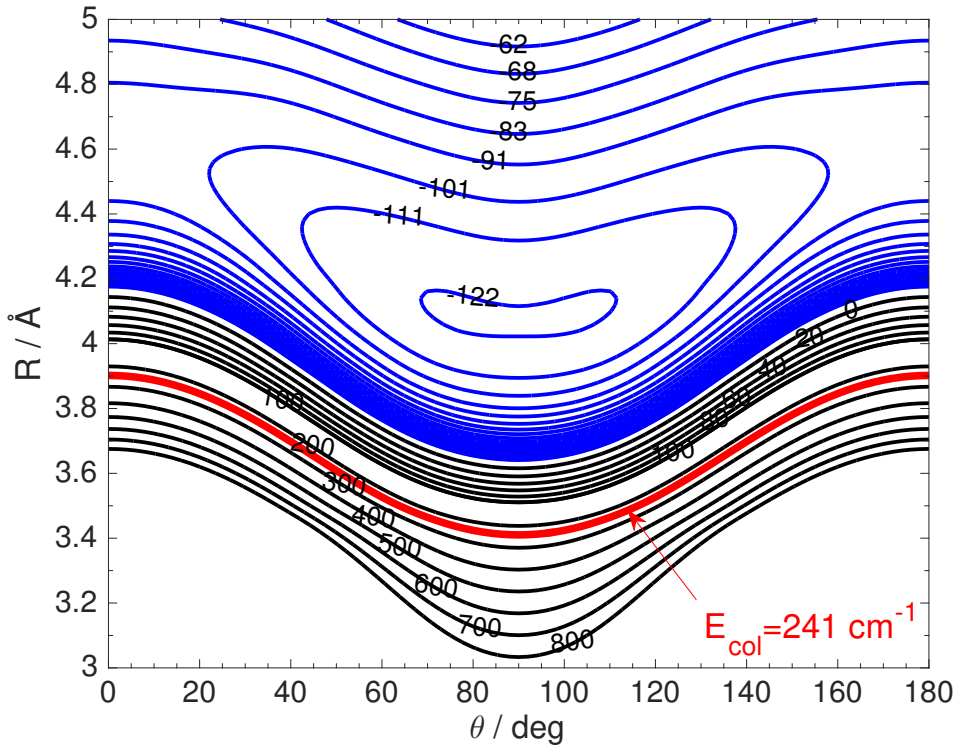

Figure 3: Contour diagram of the classical Xe-N_2 potential energy surface employed in the molecular dynamics calculations. As indicated by the labeled contours, black lines represent positive values (repulsive part of the potential); blue lines are negative values. The contour line in red represent the collision energy of the present study.

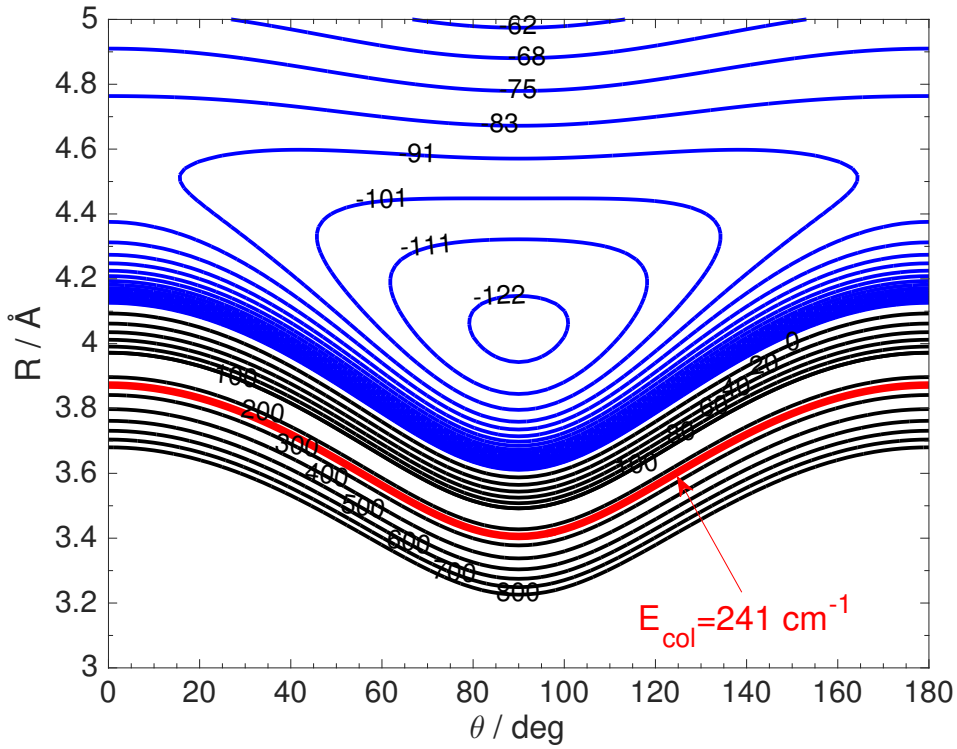

Figure 4: Comparison of the quantum mechanical [28] and classical Xe-N_2 interaction potential from this work at a collision energy of 241 cm^{-1}.

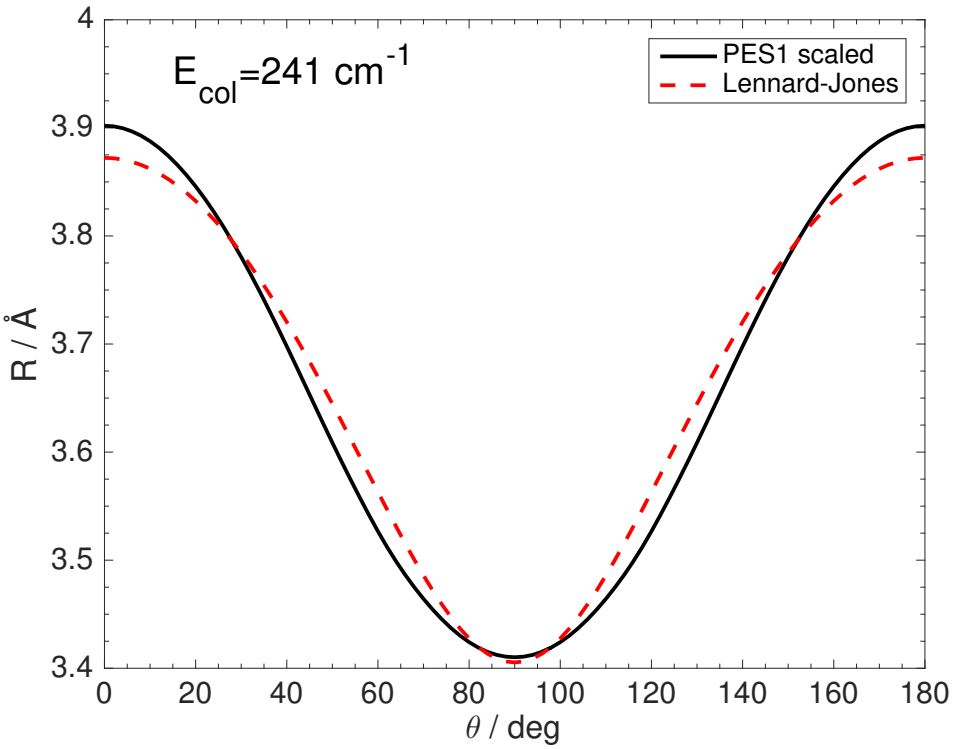

Figure 5: Pair distribution functions (PDF) for the N_2 - N_2 centre-of-mass (black solid line), N - N_2 centre-of-mass (blue, dash-dotted) and N - N (red, dotted) separations of Xe-N_2 mixture at N_2 mole fractions of 0.20 (upper panel), 0.50 (middle panel), and 0.95 (lower panel). The total concentrations are shown on the top of each column.

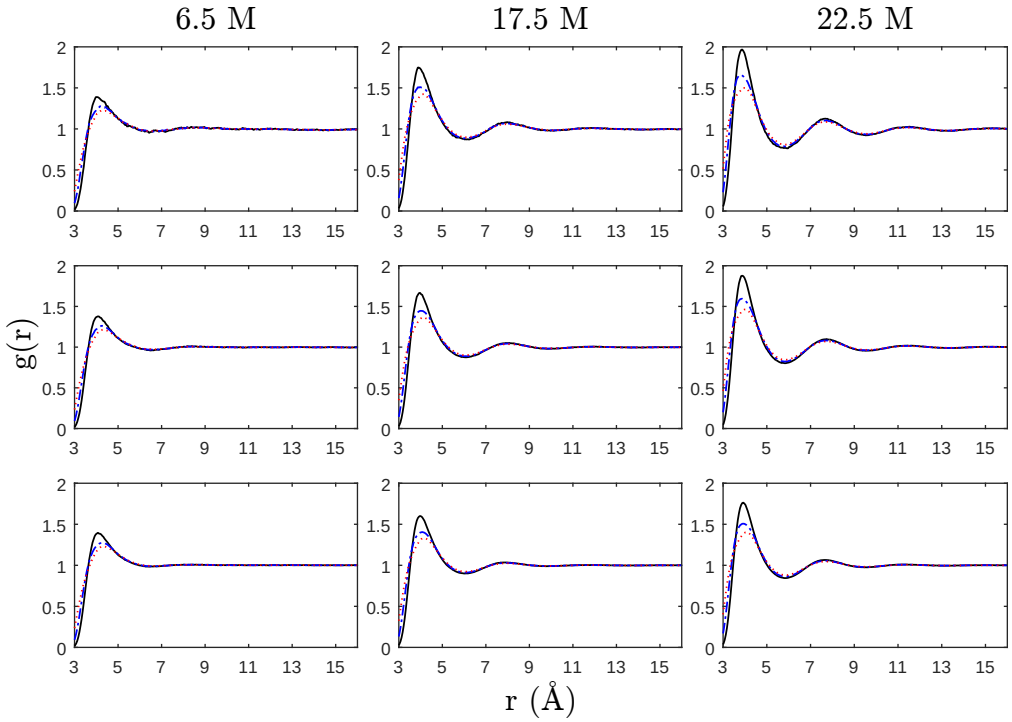

Figure 6: Pair distribution functions (PDF) for the Xe - N_2 centre-of-mass (black solid line), Xe - N (blue, dash-dotted), and Xe - Xe (red, dotted) separations of Xe-N_2 mixture at N_2 mole fractions of 0.20 (upper panel), 0.50 (middle panel), and 0.95 (lower panel). The total concentrations are shown on the top of each column.

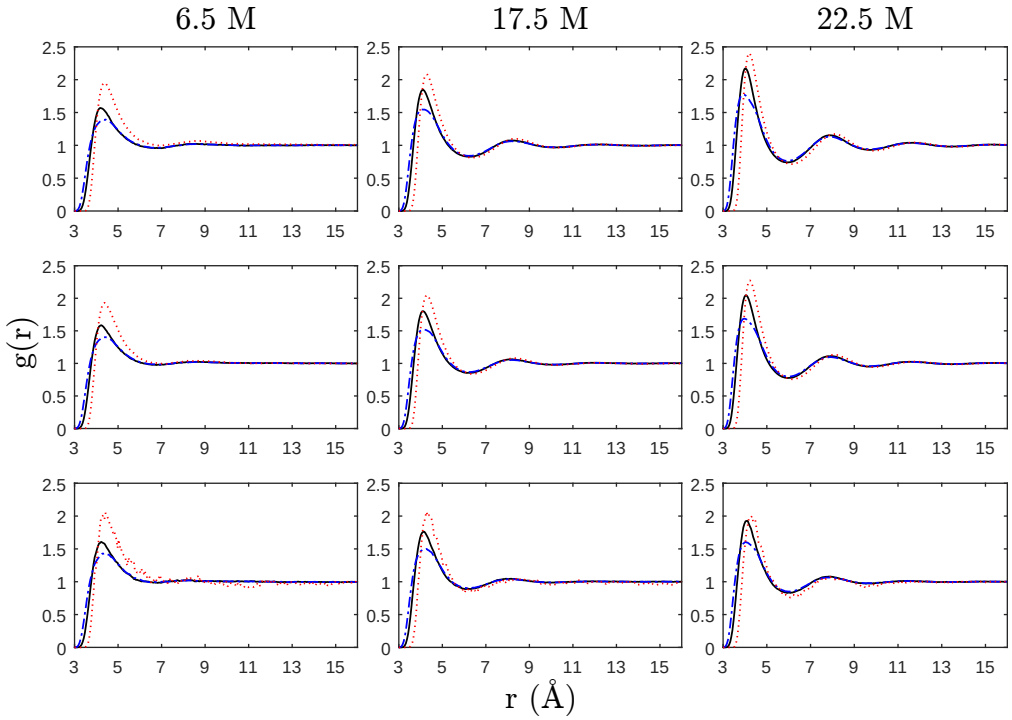

Figure 7: Experimental Rayleigh spectrum [2] of Xe-N_2 mixture for x_{N_2} = 0.2 at temperature of T = 323 K and total concentrations (M) 22.5 (black line), 17.5 (red), 12.5 (green), 6.5 (blue) and 2.75 (cyan).

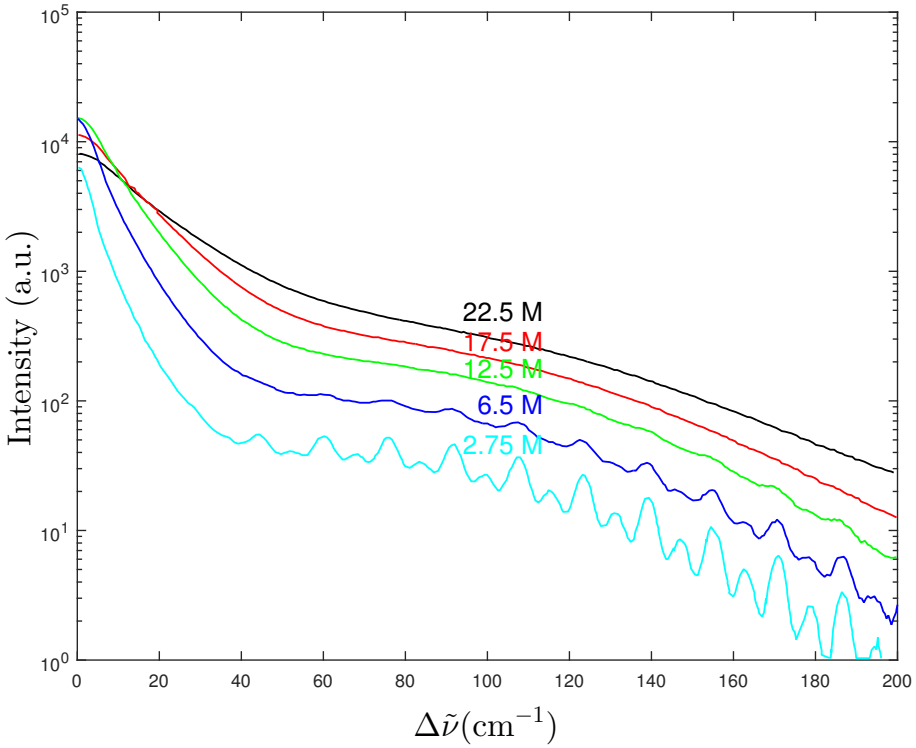

Figure 8: Comparison between experimental (circles) and MD (lines) Rayleigh TCFs of Xe-N_2 mixture at temperature of T = 323 K for concentration of 6.5M at x_{N_2} = 0.20 (black, solid line), 0.35 (blue, dash-dotted line), 0.50 (red, dotted line), 0.77 (magenta, dashed line).

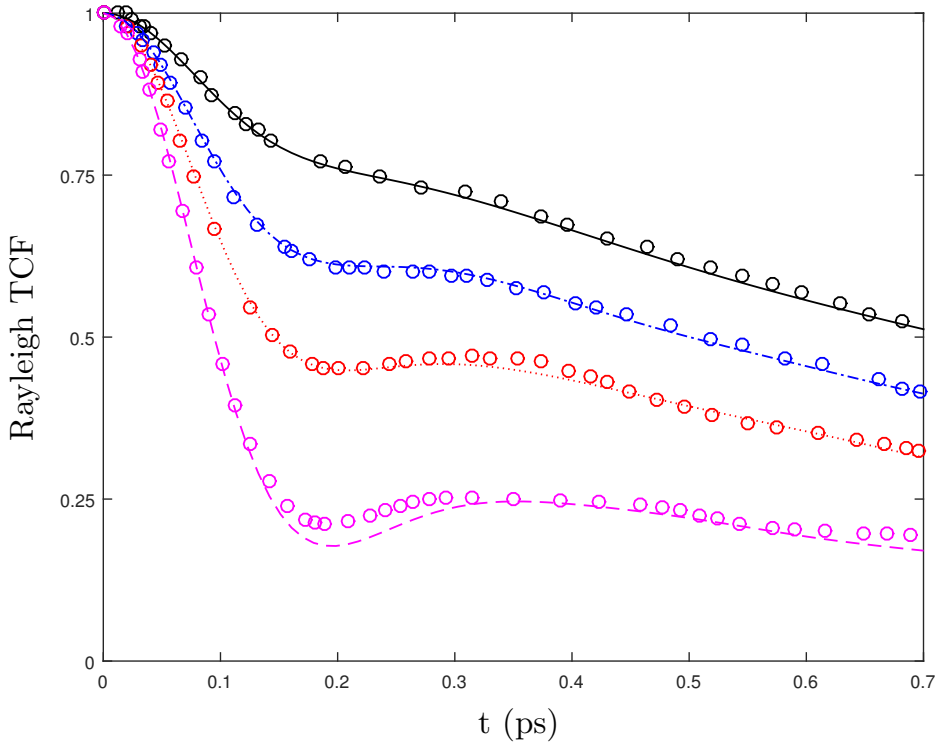

Figure 9: Total (black solid line), re-orientational (OR, blue, dash-dotted), collision-induced (CI, red, dotted), cross (CR, magenta, dashed) MD TCFs for the Rayleigh spectrum of Xe-N_2 mixture at various mole fractions and total concentrations. The concentrations are shown on the top of each column, and the nitrogen mole fractions at the left of each row.

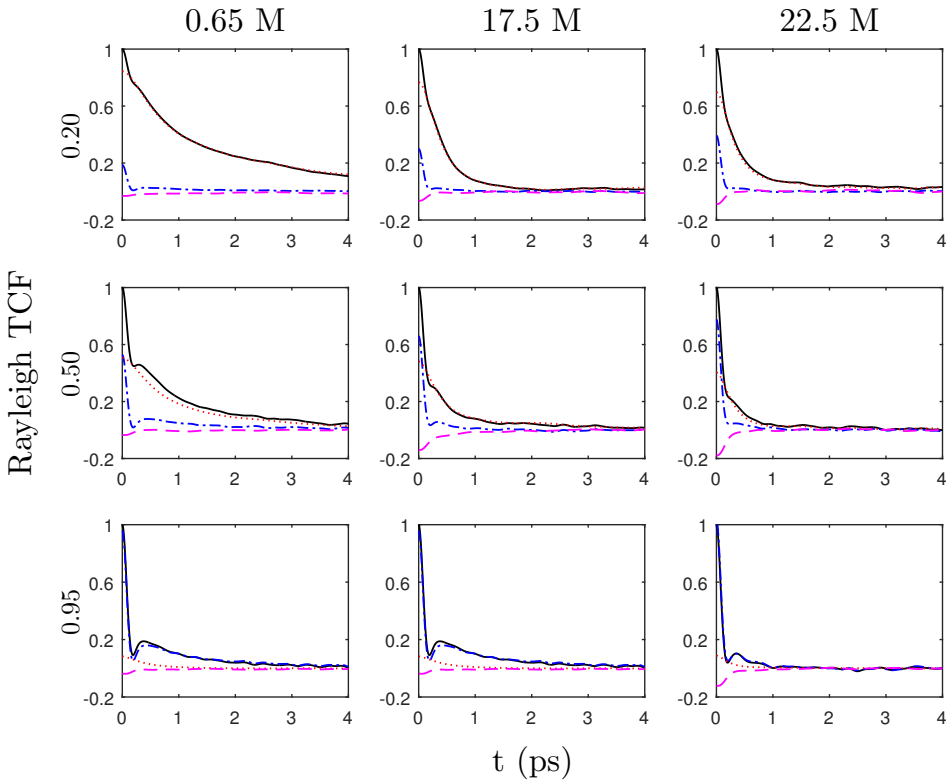

Figure 10: Comparison of calculated ICS for Xe + *ortho*-N_2 (υ = 0, J = 0, 2) (filled and empty blue squares, respectively) and Xe + *para*-N_2 (υ = 0, J = 1, 3) (filled and empty red circles, respectively) as a function of the final N_2 level at a collision energy of 241 cm^{-1}.

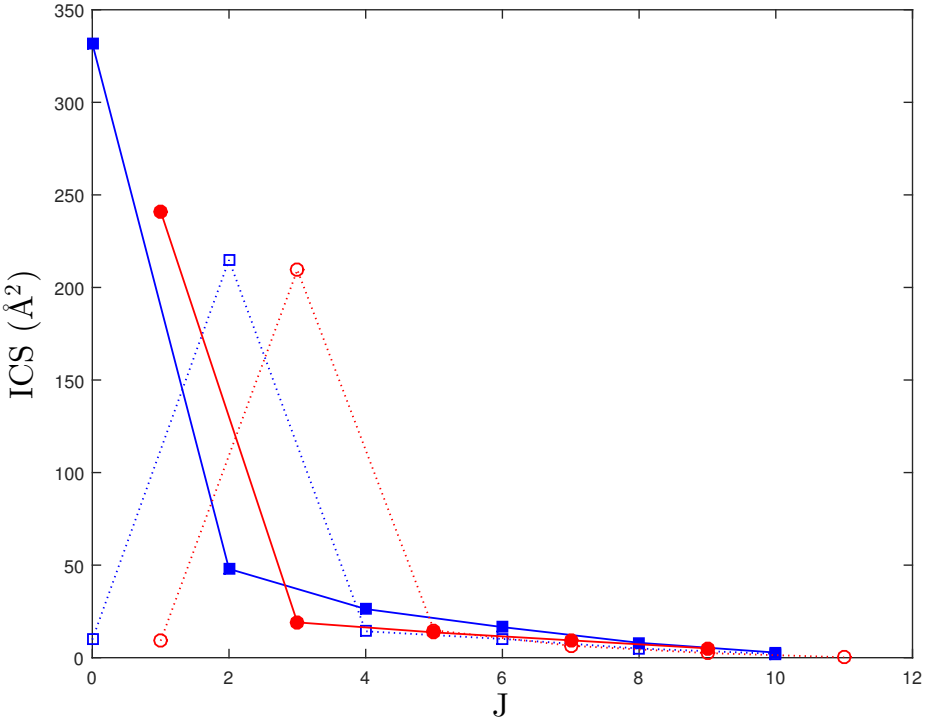

Figure 11: Left panel: comparison of calculated DCS for Xe + *ortho*-N_2 ($\upsilon = 0$, $J = 0$) collisions to final N_2 levels $J = 0$ (black), 2 (blue), and 4 (red). Right panel: as previously, but for Xe + *para*-N_2 ($\upsilon = 0$, $J = 1$) collision to final N_2 levels $J = 1$ (black), 3 (blue), and 5 (red). The collision energy is 241 cm^{-1} in all cases.